Mineralogical Magazine, June 2015, Vol. 79(3), pp. 715–733

Kerimasite, $\{Ca_3\}[Zr_2](SiFe^{3+}_2)O_{12}$ garnet from the Vysoká-Zlatno skarn, Štiavnica stratovolcano, Slovakia

PAVEL UHER[1,*], STANISLAVA MILOVSKÁ[2], RASTISLAV MILOVSKÝ[2], PETER KODĚRA[3], PETER BAČÍK[1] AND VLADIMÍR BILOHUŠČIN[1]

[1] Department of Mineralogy and Petrology, Comenius University, Mlynská dolina G, 842 15 Bratislava, Slovakia
[2] Geological Institute, Slovak Academy of Sciences, Banská Bystrica branch, Ďumbierska 1, 974 01 Banská Bystrica, Slovakia
[3] Department of Geology of Mineral Deposits, Comenius University, Mlynská dolina G, 842 15 Bratislava, Slovakia

[*Received 5 August 2014; Accepted 2 December 2014; Associate Editor: E. Grew*]

ABSTRACT

Kerimasite $\{Ca_3\}[Zr_2](SiFe^{3+}_2)O_{12}$, a rare member of the garnet supergroup, has been identified in association with andradite–grossular and their hydrated analogues, monticellite, perovskite, clintonite, anhydrite, hydroxylellestadite–fluorellestadite, spinel, magnetite, brucite, valeriite and other minerals from a Ca-Mg skarn in the exocontact of a granodiorite porphyry intrusion in Vysoká-Zlatno Cu-Au skarn-porphyry deposit, the Štiavnica stratovolcano, Central Slovakia. Kerimasite forms euhedral-to-anhedral crystals, 2 to 100 μm across with 0.73–1.62 atoms per formula unit (a.p.f.u.) Zr (16.2–33.6 wt.% ZrO_2), 0.34–0.66 a.p.f.u. Ti (4.6–9.3 wt.% TiO_2), 0.01 to 0.05 a.p.f.u. Hf (0.4–1.7 wt.% HfO_2: the largest Hf content reported in kerimasite), and small amounts of Sn, Sc and Nb ($\leqslant$0.02 a.p.f.u.). Tetrahedral Si (0.99–1.67 a.p.f.u.; 9.8–18.1 wt.% SiO_2) is balanced by 0.85–1.26 a.p.f.u. $Fe^{3+}$and by 0.46–0.76 a.p.f.u. Al. The crystals commonly show regular, oscillatory concentric zoning or irregular patchy internal textures due to Zr, Ti, Fe, Al and Si variations during growth or partial alteration and dissolution-reprecipitation. The main substitutions in kerimasite are $^{Y}(Fe,Sc)^{3+} + {}^{Z}Si^{4+} = {}^{Y}(Zr,Ti,Hf,Sn)^{4+} + {}^{Z}(Fe,Al)^{3+}$ and $Ti^{4+} = Zr^{4+}$. Associated andradite locally contains irregular Ti- and Zr-rich zones with $\leqslant$11 wt.% TiO_2 and $\leqslant$4.4 wt.% ZrO_2. In comparison with common Ca-rich garnets, the micro-Raman spectrum of kerimasite shows that many bands shift towards much lower wavenumbers, either due to Fe^{3+} substitution on the *Z* site or to the strong influence of neighbouring octahedrally-coordinated Zr^{4+} on internal vibrations of tetrahedra that share oxygens. The formation of kerimasite, monticellite, perovskite and other phases indicate a relatively Ca-rich and Si,Al-poor environment, analogous to other known occurrences of Ca-Zr garnets (Ca-rich skarns and xenoliths, carbonatites). Kerimasite and associated skarn minerals originated during contact-thermal metamorphism of Upper Triassic marl slates with limestone, dolomite, anhydrite and gypsum by Miocene granodiorite porphyry at $T \approx 700$ºC and $P \approx 50$–70 MPa.

KEYWORDS: kerimasite, garnet, skarn, electron microprobe, micro-Raman, contact thermal metamorphism, Cu-Au skarn-porphyry deposit, Štiavnica stratovolcano, Slovakia.

Introduction

ZIRCONIUM and titanium belong to the most common tetravalent elements occupying the octahedral *Y* site of the garnet supergroup minerals (Grew *et al.*, 2013). Their concentration is usually small (<1 wt.%) in common ^{Y}Al-dominant members (almandine, spessartine, pyrope), whereas Ca-rich garnets could be enriched markedly in Zr and Ti (e.g. Milton *et al.*, 1961; Koritnig *et al.*, 1978; Platt and Mitchell, 1979; Munno *et al.*, 1980; Lupini *et al.*, 1992; Ulrych *et al.*, 1994; Jamtveit *et al.*, 1997; Gwalani *et al.*, 2000; Schingaro *et al.*, 2001; Haynes *et al.*,

* E-mail: puher@fns.uniba.sk
DOI: 10.1180/minmag.2015.079.3.15

2003; Galuskin, 2005; Chakhmouradian and McCammon, 2005; Galuskina *et al.*, 2005, 2010*a*–*d*, 2013*a*,*b*; Katerinopoulou *et al.*, 2009; Zaitsev *et al.*, 2010). All these Ti and Zr species originated in specific natural conditions, generally enriched in Ca, Ti and Zr but poor in Al and Si, such as alkaline magmatic suites, carbonatites, lamprophyre dykes, or metamorphic/metasomatic carbonatic lithologies, especially skarns, rodingites and Ca-rich xenoliths in volcanic rocks. Hutcheonite is reported from the Allende carbonaceous chondrite (Ma and Krot, 2014). Recently, three Ti-dominant and four Zr-dominant garnet species have been described and defined (Grew *et al.*, 2013 and references therein; Ma and Krot, 2014): usturite, elbrusite, hutcheonite, kimzeyite, schorlomite, kerimasite and morimotoite (Table 1).

Kerimasite, ideally $\{Ca_3\}[Zr_2](SiFe^{3+}_2)O_{12}$, represents a rare member of the garnet supergroup, described only recently from carbonatite rocks of the Kerimasi volcano and surrounding explosion craters (Tanzania) in the East-Africa rift system (Zaitsev *et al.*, 2010). However, the Zr,Ti-rich garnets consisting of kerimasite–kimzeyite–schorlomite solid solution (kerimasite was formerly known as "Fe^{3+}-kimzeyite") were also reported from carbonate-rich lamprophyre from Marathon Dikes, Ontario, Canada (Platt and Mitchell, 1979), the Magnet Cove carbonatite, Arkansas, USA (Lupini *et al.*, 1992; Haynes *et al.*, 2003), Polino carbonatite, Italy (Lupini *et al.*, 1992), melilitic volcanic ejecta from Anguillara Sabazia, Italy (Schingaro *et al.*, 2001), rodingite-like rocks from Wiluy River, Sakha (Yakutia), Russia (Galuskin, 2005; Galuskina *et al.*, 2005, 2010*a*) and carbonate-silicic skarn xenoliths from the Upper Chegem Caldera, Kabardino-Balkaria, Russia (Galuskina *et al.*, 2010*b*–*d*, 2013*a*,*b*).

However, kerimasite occurrences are rare and our knowledge about this mineral is still limited. Consequently, here we present a detailed description of kerimasite in a contact-metamorphic skarn mineral assemblage from the Vysoká-Zlatno Cu-Au skarn-porphyry deposit, central Slovakia. Compositional variations, results of micro-Raman spectroscopy and genetic conditions of kerimasite from this locality are described and discussed in our contribution.

Regional geology and sample location

The Vysoká-Zlatno Cu-Au skarn-porphyry deposit occurs in the western part of the central zone of the Štiavnica stratovolcano, hosted by the Central Slovakia Neogene Volcanic Field, located on the inner side of the Carpathian arc. The Cu-Au skarn-porphyry mineralization in this district is related to granodiorite and quartz-diorite porphyry dyke clusters and stocks (Lexa *et al.*, 1999; Koděra *et al.*, 2010). The porphyry intrusion of granodiorite to quartz diorite belongs to the Zlatno Intrusive Complex of the second evolution stage of the Štiavnica stratovolcano; the plutonic rocks of the stratovolcano show a Miocene age of 13.3 and 13.4 ±0.2 Ma according to Rb-Sr whole-rock mineral isochrons (Chernyshev *et al.*, 2013), in accordance with the U-Th-Pb zircon dating by sensitive high-resolution ion microprobe (SHRIMP; ~13 Ma, Kohút and Danišík, 2013). Major Cu-Au mineralization overlaps with the zone of skarns at contacts between the biotite-amphibole granodiorite porphyry stock and Upper Triassic sediments rich in carbonates (limestones, dolomites) and evaporites (anhydrite, gypsum) of the Veký Bok Group (Koděra *et al.*, 2010).

TABLE 1. End-member formulae and classification of Zr- and Ti-bearing members of the garnet supergroup (Grew *et al.*, 2013; Ma and Krot, 2014).

Member	Formula	Group	Class
Usturite	$\{Ca_3\}[Sb^{5+}Zr](Fe^{3+}_3)O_{12}$	Bitikleite	Oxide
Elbrusite	$\{Ca_3\}[U^{6+}_{0.5}Zr_{1.5}](Fe^{3+}_3)O_{12}$	Bitikleite	Oxide
Hutcheonite	$\{Ca_3\}[Ti_2](SiAl_2)O_{12}$	Schorlomite	Silicate
Kimzeyite	$\{Ca_3\}[Zr_2](SiAl_2)O_{12}$	Schorlomite	Silicate
Schorlomite	$\{Ca_3\}[Ti_2](SiFe^{3+}_2)O_{12}$	Schorlomite	Silicate
Kerimasite	$\{Ca_3\}[Zr_2](SiFe^{3+}_2)O_{12}$	Schorlomite	Silicate
Morimotoite	$\{Ca_3\}[TiFe^{2+}](Si_3)O_{12}$	Garnet	Silicate

https://doi.org/10.1180/minmag.2015.079.3.15 Published online by Cambridge University Press

The skarn mineralization is of Mg-Ca type, developed in both altered dolomites and limestones (exoskarns) and on the margins of the granodiorite intrusion (endoskarns) at depths of ~670 to 1000 m (Burian and Smolka, 1982). The skarn rocks are represented variably by prograde and retrograde Mg- and Ca-skarn mineral assemblages (Koděra *et al.*, 2010); major prograde stage minerals include mainly forsterite, wollastonite, diopside, garnet (andradite-grossular), monticellite, spinel, Mg-rich magnetite and ilmenite. Retrograde mineral assemblages could be subdivided into (1) an older, higher-temperature substage with phlogopite and chlorite accompanied by actinolite-tremolite, clintonite, epidote, titanite and vesuvianite and (2) a younger, lower-temperature substage with talc, serpentinite, brucite, hydroxylellestadite, anhydrite and carbonates with magnetite, hematite, sulfide minerals (pyrrhotite, pyrite, chalcopyrite, sphalerite, molybdenite) and rare gold (Koděra *et al.*, 2010 and references therein).

In the present study, kerimasite and associated minerals have been studied from a sample of Mg-Ca skarn from the R-1 borehole, from a depth of 677 m, located on the northern margin of the Vysoká-Zlatno Cu-Au skarn-porphyry deposit (sample R-1/677). The borehole is situated in the eastern slope of the Zlatno Valley, ~2 km northwest of the Vysoká village and ~10 km southwest of the Banská Štiavnica town, central Slovakia. Geographical coordinates of the R-1 borehole are: 48º25′42″ N 18º46′20″ E.

Analytical methods

Polished thin sections of the rock were studied under a polarizing microscope. Chemical compositions and internal zoning of minerals were investigated using the CAMECA SX 100 wavelength electron microprobe housed at the Dionýz Štúr State Geological Institute, Bratislava. Analytical conditions were 15 kV accelerating voltage, 20 nA sample current and a 1–3 μm beam diameter for garnet and associated minerals. The following standards and spectral lines were used for calibration: apatite (P*K*α), ferrocolumbite (Nb*L*α), manganotantalite (Ta*L*α), orthoclase (Si*K*α, K*K*α), TiO_2 (Ti*K*α), $ZrSiO_4$ (Zr*L*α), HfO_2 (Hf*L*α), Al_2O_3 (Al*K*α), metallic Cr (Cr*K*α), $ScPO_4$ (Sc*K*α), YPO_4, (Y*L*α), fayalite (Fe*K*α), rhodonite (Mn*K*α), willemite (Zn*K*α), forsterite (Mg*K*α), wollastonite (Ca*K*α), albite (Na*K*α), LiF (F*K*α) and NaCl (Cl*K*α). The detection limits of the measured elements were 0.02–0.08 wt.%. Examination of energy dispersive spectroscopy data revealed no measurable concentrations of other cations reported in garnet such as As, U, V, Sb, rare earth elements and Zn in the kerimasite studied. Moreover, measured amounts of Mn, Na, F and Cl concentrations are usually below the detection limit of the electron microprobe. The matrix effects were corrected using the *PAP* procedure of Pouchou and Pichoir (1985).

Micro-Raman spectra were measured using a LabramHR (Horiba Jobin-Yvon) microspectrometer, based on an Olympus BX41 microscope with a confocally coupled Czerny-Turner type monochromator (focal length 800 mm) at the Geological Institute, Slovak Academy of Sciences, Banská Bystrica. A polarized laser emission at $\lambda = 532$ nm was used for excitation (frequency-doubled Nd:YAG laser). No shift of peak positions due to thermal effects was observed when excited through a series of neutral density filters, which justified excitation with full power at ~200 mW on the sample. The Raman-scattered light was collected in 180º geometry through a 100× objective lens with numerical aperture of 0.8 and dispersed by diffraction grating with a density of 1800 $g.mm^{-1}$ onto a cooled CCD detector, exposure time was 200 s. The measurement accuracy was verified using emission lines of a neon glow lamp. Possible artifacts and photoluminescence peaks were excluded after comparison with spectra excited by a 633 nm laser line. The Raman spectrum was acquired in the range 50–4000 cm^{-1} in order to check for the presence of hydroxyl/water in the structure. Peak fitting and deconvolution was performed with the *PeakFit*® program (SeaSolve Software Inc.), spectra were fitted to the minimum number of Gauss-Lorentzian components to accurately match the measured curve. Raman tensors were calculated on the Bilbao crystallographic server (Aroyo *et al.*, 2006*a*,*b*; 2011; Kroumova *et al.*, 2003) using crystallographic data from the American Mineralogist Crystal Structure Database (Downs and Hall-Wallace, 2003).

Results

Kerimasite occurrence

Kerimasite garnet occurs as a rare accessory mineral in the monticellite-rich skarn rock. Under the optical microscope, kerimasite shows transparent isometric crystals with pale yellow colour and high positive relief (Fig. 1), without apparent

https://doi.org/10.1180/minmag.2015.079.3.15 Published online by Cambridge University Press

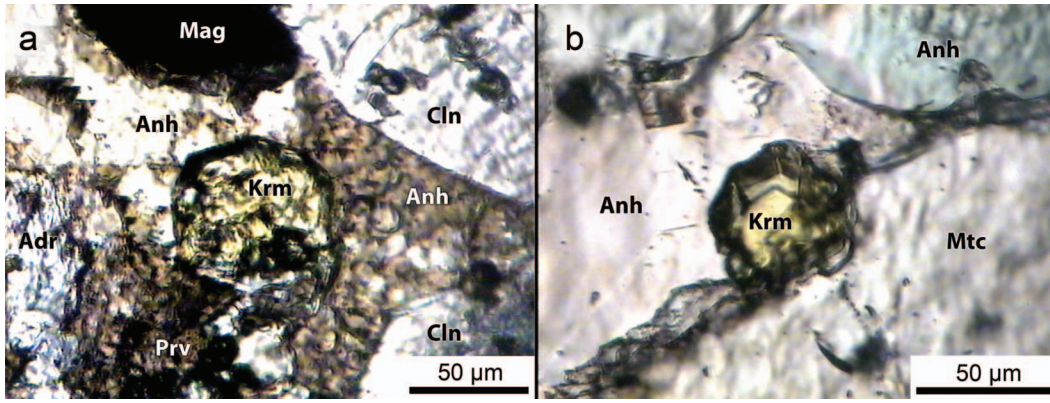

FIG. 1. (*a,b*) Photomicrographs (plane-polarized light) of kerimasite crystals (yellow, centre) from the Vysoká-Zlatno skarn. Mineral abbreviations: Krm – kerimasite, Adr – andradite, Anh – anhydrite, Cln – clintonite, Mag – magnetite, Mtc – monticellite; Prv – perovskite.

anomalous birefrigence in crossed polars. Kerimasite usually forms individual euhedral-to-anhedral crystals, 20 μm to ~100 μm across in andradite–grossular, monticellite, clintonite and anhydrite, in association with perovskite, spinel, Mg-rich magnetite (~5 wt.% MgO), hydroxylellestadite–fluorellestadite, brucite, valleriite and other minerals (Figs 1, 2*a,b*). Locally, irregular intergrowths or overgrowths of andradite–grossular and perovskite on kerimasite are present (Fig. 2*b*). Rarely, kerimasite occurs as tiny (<10 μm) anhedral skeletal-like crystals or irregular inclusions in massive zonal andradite (Fig. 2*c*). Detailed descriptions of associated monticellite, clintonite, hydroxylellestadite–fluorellestadite and perovskite are included in papers by Koděra *et al.* (2009) and Uher *et al.* (2011).

Kerimasite composition

Crystals of kerimasite show regular, oscillatory concentric zoning or irregular patchy internal textures (Fig. 2*d–f*). Both regular and irregular zoning display variations of Zr, Ti, Fe, Al and Si during the growth or partial alteration and dissolution-reprecipitation: the pale zones show enrichment in Zr and Al, whereas the dark ones reveal larger amounts of Ti, Fe and Si.

Over 40 electron-microprobe analyses of 18 individual crystals of kerimasite reveal an extensive compostional variation (Table 2). Totals of kerimasite electron-microprobe analyses are usually close to 100 ± 1 wt.%. The results of the micro-Raman spectroscopy (see the next section) indicate the absence or an insignificant amount of the hydroxyl anion. Consequently, the kerimasite formulae were calculated on the basis of 12 oxygen anions, 8 cations and a charge-balance calculation which enabled the estimation of Fe^{3+} and Fe^{2+} (Fe_2O_3 *vs.* FeO) contents. The site allocations were calculated according to the procedure of Grew *et al.* (2013).

The *X* site position of kerimasite formulae is occupied almost entirely by calcium. Only negligible amounts of Sr were detected locally ($\leqslant$0.006 a.p.f.u., $\leqslant$0.1 wt.% SrO).

Zirconium is a dominant element of the octahedral *Y* site of the kerimasite studied; it has 0.73 to 1.62 a.p.f.u. (16.2 to 33.6 wt.% ZrO_2). Titanium concentrations are distinctly smaller, they have 0.34 to 0.66 a.p.f.u. (4.6 to 9.3 wt.% TiO_2) and atomic ratio Zr/(Zr+Ti) = 0.53–0.83. Calculated contents of $^{Y}Fe^{3+}$ show wide variations (0.00 to 0.50 a.p.f.u.), whereas estimates of ^{Y}Al contents indicate its absence from the *Y* site. Minor contents of Hf, Sn, Sc and Nb are also characteristic of the kerimasite investigated; they reach 0.01 to 0.05 a.p.f.u. Hf (0.4 to 1.7 wt.% HfO_2), up to 0.02 a.p.f.u. Sn ($\leqslant$0.45 wt.% SnO_2), up to 0.02 a.p.f.u. Sc ($\leqslant$0.29 wt.% Sc_2O_3) and up to 0.01 a.p.f.u. Nb ($\leqslant$0.23 wt.% Nb_2O_5). Concentrations of other measured elements (Ta, Cr and Mg) are usually close to or below the detection limits of the electron microprobe.

The tetrahedral *Z* site of the kerimasite studied is occupied by Si, Fe^{3+} and Al. Contents of Si (0.99 to 1.67 a.p.f.u.; 9.8 to 18.1 wt.% SiO_2) are balanced by 0.85 to 1.26 a.p.f.u. $Fe^{3+}$and by 0.46 to 0.76 a.p.f.u. Al. Phosphorus shows only trace concentrations (<0.1 wt.% P_2O_5).

https://doi.org/10.1180/minmag.2015.079.3.15 Published online by Cambridge University Press

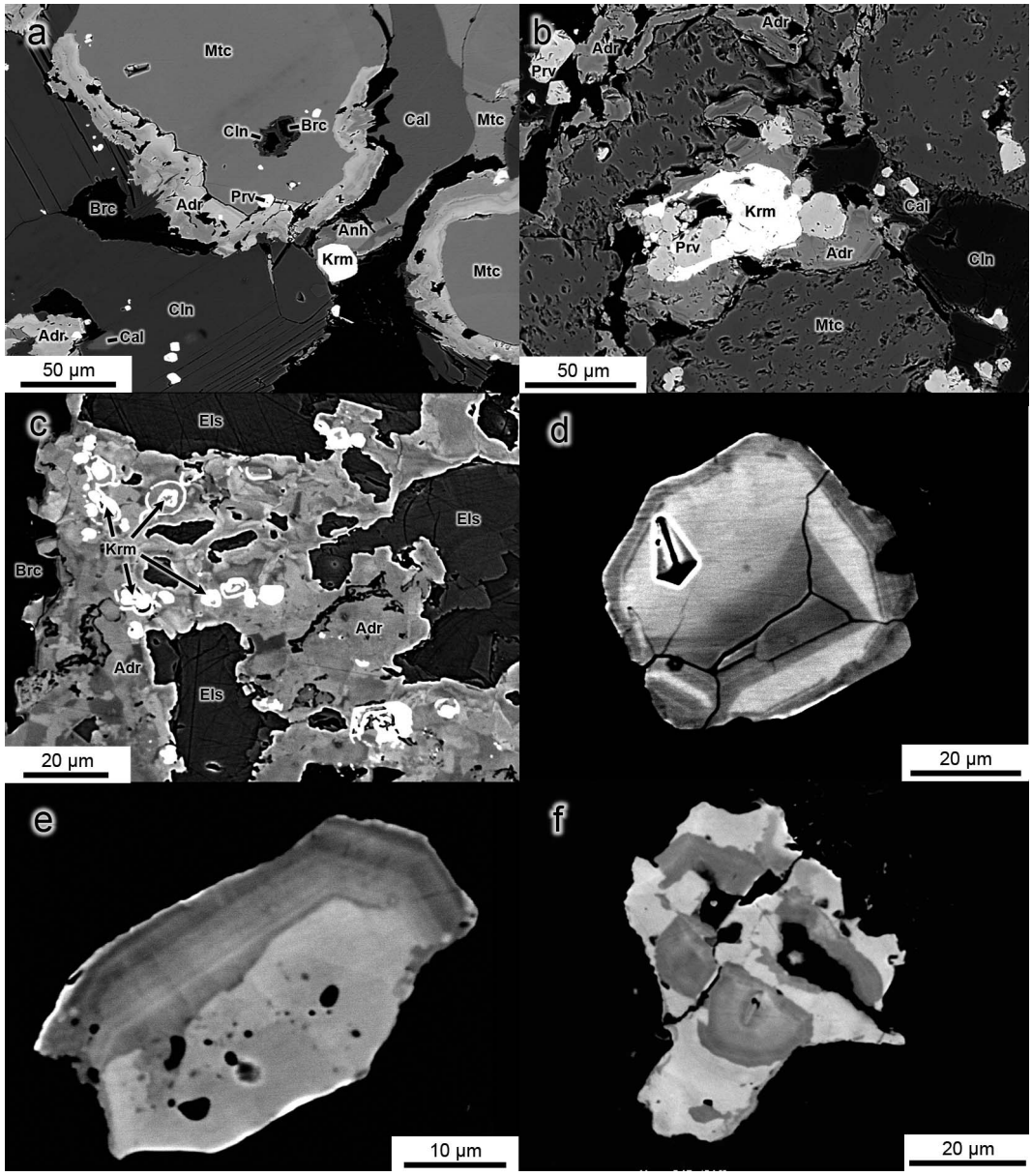

FIG. 2. Backscattered electron images of kerimasite and associated minerals from the Vysoká-Zlatno skarn. Mineral abbreviations: Adr – andradite-grossular, Anh – anhydrite, Brc – brucite, Cal – calcite, Cln – clintonite, Els – ellestadite, Krm – kerimasite, Mtc – monticellite, Prv – perovskite; (*a*) small kerimasite crystal in association with anhydrite, andradite, brucite, monticellite, clintonite, calcite and perovskite; (*b*) kerimasite–perovskite intergrowth with andradite and associated minerals; (*c*) irregular skeletal atoll-like kerimasite crystals in andradite with associated ellestadite and brucite; (*d–e*) crystals of kerimasite showing regular, fine oscillatory concentric zoning; (*f*) anhedral kerimasite grain with an irregular patchy internal texture.

https://doi.org/10.1180/minmag.2015.079.3.15 Published online by Cambridge University Press

TABLE 2. Representative electron-microprobe compositions (wt.%) of kerimasite from the Vysoká-Zlatno skarn.

Sample #	R1B41C	R1B04E	R1B06E	R1C16D	R1A07E	R1B07D	R1C02E	R1C04E	R1C11D	R1C15D	R1C01E	R1C03E	R1B05D	R1A04C	R1C10D	R1A06E
P_2O_5	0.03	0.03	0.00	0.00	0.00	0.00	0.00	0.06	0.03	0.06	0.00	0.03	0.05	0.04	0.00	0.00
Nb_2O_5	0.16	0.19	0.18	0.16	0.15	0.13	0.13	0.08	0.16	0.13	0.15	0.13	0.17	0.19	0.20	0.13
Ta_2O_5	0.03	0.00	0.00	0.06	0.00	0.04	0.00	0.08	0.10	0.00	0.00	0.00	0.07	0.08	0.00	0.00
SiO_2	18.05	17.89	15.13	13.36	13.16	12.72	12.21	12.15	11.21	10.90	10.79	10.57	10.26	10.08	9.84	10.04
TiO_2	9.34	8.55	8.87	6.58	5.65	6.22	6.07	6.36	5.31	4.96	5.47	5.63	4.78	4.69	4.72	4.78
ZrO_2	16.19	17.97	21.11	24.69	26.90	27.02	27.90	28.83	30.21	30.67	31.06	31.28	32.01	32.80	32.86	33.55
HfO_2	0.61	0.64	0.77	0.73	0.62	0.61	0.99	0.67	0.67	0.59	1.50	1.74	0.74	0.78	0.83	0.74
SnO_2	0.24	0.28	0.28	0.17	0.12	0.18	0.29	0.18	0.15	0.19	0.35	0.45	0.20	0.13	0.19	0.16
Al_2O_3	4.35	4.26	5.29	4.99	4.69	5.28	5.27	5.67	5.72	5.92	6.00	6.36	6.17	6.11	6.38	6.24
Cr_2O_3	0.00	0.00	0.00	0.03	0.03	0.00	0.00	0.00	0.00	0.03	0.00	0.00	0.00	0.00	0.00	0.04
Sc_2O_3	0.21	0.24	0.16	0.18	0.13	0.14	0.12	0.11	0.08	0.11	0.09	0.09	0.10	0.07	0.04	0.06
Y_2O_3	0.00	0.05	0.00	0.06	0.05	0.00	0.00	0.00	0.03	0.00	0.00	0.04	0.03	0.03	0.04	0.00
Fe_2O_3	19.77	18.70	17.83	18.27	18.50	17.79	18.31	17.19	16.65	16.89	16.53	16.11	16.47	16.69	16.22	16.63
FeO	0.04	0.72	0.49	0.00	0.07	0.00	0.13	0.57	0.20	0.00	0.21	0.29	0.14	0.00	0.00	0.04
MnO	0.04	0.00	0.00	0.04	0.03	0.00	0.00	0.00	0.00	0.00	0.04	0.00	0.00	0.00	0.00	0.00
MgO	0.11	0.24	0.00	0.00	0.00	0.00	0.00	0.00	0.00	0.00	0.00	0.00	0.00	0.00	0.00	0.00
CaO	30.98	30.46	30.03	28.97	28.61	28.77	28.71	28.93	28.25	28.11	28.47	28.59	27.76	28.40	28.08	28.29
SrO	0.05	0.00	0.00	0.06	0.05	0.00	0.04	0.00	0.00	0.06	0.07	0.05	0.10	0.06	0.06	0.07
Na_2O	0.00	0.00	0.00	0.00	0.03	0.04	0.00	0.00	0.00	0.00	0.00	0.00	0.03	0.00	0.00	0.00
Total	100.20	100.22	100.14	98.35	98.79	98.94	100.17	100.88	98.77	98.62	100.73	101.36	99.08	100.15	99.46	100.77
Formulae based on 12 oxygen anions, 8 cations and valence calculations																
P	0.002	0.002	0.000	0.000	0.000	0.000	0.000	0.005	0.003	0.005	0.000	0.002	0.004	0.003	0.000	0.000
Si	1.660	1.656	1.426	1.310	1.296	1.248	1.194	1.178	1.120	1.092	1.065	1.038	1.031	1.005	0.988	0.996
Al *Z*	0.472	0.465	0.588	0.577	0.544	0.611	0.607	0.648	0.673	0.699	0.698	0.736	0.731	0.718	0.755	0.729
Fe^{3+} *Z*	0.866	0.877	0.986	1.113	1.160	1.141	1.199	1.169	1.204	1.204	1.228	1.191	1.234	1.253	1.226	1.241
Sum *Z*	3.000	3.000	3.000	3.000	3.000	3.000	3.000	3.000	3.000	3.000	2.991	2.967	3.000	2.979	2.969	2.966
Nb	0.007	0.008	0.008	0.007	0.007	0.006	0.006	0.004	0.007	0.006	0.007	0.006	0.008	0.009	0.009	0.006
Ta	0.001	0.000	0.000	0.002	0.000	0.001	0.000	0.002	0.003	0.000	0.000	0.000	0.002	0.002	0.000	0.000
Ti	0.646	0.595	0.629	0.485	0.418	0.459	0.446	0.464	0.399	0.374	0.406	0.416	0.361	0.352	0.357	0.356
Zr	0.726	0.811	0.970	1.181	1.291	1.293	1.330	1.362	1.471	1.498	1.495	1.498	1.568	1.595	1.609	1.622
Hf	0.016	0.017	0.021	0.020	0.017	0.017	0.028	0.019	0.019	0.017	0.042	0.049	0.021	0.022	0.024	0.021
Sn	0.009	0.010	0.011	0.007	0.005	0.007	0.011	0.007	0.006	0.008	0.014	0.018	0.008	0.005	0.008	0.006
Al *Y*	0.000	0.000	0.000	0.000	0.000	0.000	0.000	0.000	0.000	0.000	0.000	0.000	0.000	0.000	0.000	0.000
Cr	0.000	0.000	0.000	0.002	0.002	0.000	0.000	0.000	0.000	0.002	0.000	0.000	0.000	0.000	0.000	0.003
Sc	0.017	0.019	0.013	0.015	0.011	0.012	0.010	0.009	0.007	0.010	0.008	0.008	0.009	0.006	0.004	0.005

Fe^{3+} *Y*	0.502	0.426	0.279	0.236	0.210	0.173	0.148	0.085	0.047	0.069	0.000	0.000	0.011	0.000	0.000	0.000	0.000
Fe^{2+}	0.003	0.056	0.039	0.000	0.006	0.000	0.011	0.046	0.017	0.000	0.017	0.024	0.011	0.000	0.000	0.000	0.004
Mn	0.003	0.000	0.000	0.003	0.003	0.000	0.000	0.000	0.000	0.000	0.003	0.000	0.000	0.000	0.000	0.000	0.000
Mg	0.015	0.033	0.000	0.000	0.000	0.000	0.000	0.000	0.000	0.000	0.000	0.000	0.000	0.000	0.000	0.000	0.000
Sum *Y*	1.945	1.975	1.970	1.958	1.970	1.968	1.990	1.998	1.976	1.984	1.992	2.019	1.999	1.991	2.011	2.023	
Y	0.000	0.002	0.000	0.003	0.003	0.000	0.000	0.000	0.002	0.000	0.000	0.002	0.002	0.002	0.002	0.000	
Ca	3.053	3.021	3.032	3.045	3.018	3.025	3.007	3.004	3.023	3.017	3.012	3.009	2.988	3.035	3.022	3.006	
Sr	0.003	0.000	0.000	0.003	0.003	0.000	0.002	0.000	0.000	0.003	0.004	0.003	0.006	0.003	0.003	0.004	
Na	0.000	0.000	0.000	0.000	0.006	0.008	0.000	0.000	0.000	0.000	0.000	0.000	0.006	0.000	0.000	0.000	
Sum *X*	3.056	3.021	3.032	3.048	3.027	3.033	3.009	3.004	3.023	3.020	3.016	3.012	3.000	3.038	3.025	3.010	
Z $Fe^{3+}/(Fe^{3+}+Al)$	0.65	0.65	0.63	0.66	0.68	0.65	0.66	0.64	0.64	0.63	0.64	0.62	0.63	0.64	0.62	0.63	
Zr/(Zr+Ti)	0.53	0.58	0.61	0.71	0.76	0.74	0.75	0.75	0.79	0.80	0.79	0.78	0.81	0.82	0.82	0.82	

Generally, the kerimasite compositions show a distinct dominance of the $Ca_3Zr_2SiFe_2^{3+}O_{12}$ end-member (Fig. 3), however in some places the dark zones reveal compositions towards andradite or grossular (Fig. 4). The $^{Y}(Fe,Sc)^{3+} + {}^{Z}Si^{4+} = {}^{Y}(Zr,Ti,Hf,Sn)^{4+} + {}^{Z}(Fe,Al)^{3+}$ couple substitution represents the principal mechanism driving the compositional variations in the kerimasite studied (Fig. 5*a*–*d*). This complex coupled substitution is also responsible for deviation of the partial $^{Y}Ti^{4+} = {}^{Y}Zr^{4+}$ exchange vector (Fig. 5*c*).

Micro-Raman spectroscopy of kerimasite

Factor-group analysis of garnet (space group $Ia\bar{3}d$) yields 25 Raman active modes: $3A_{1g}$, $8E_g$, $14T_{2g}$. There are 14 internal stretching $(Z-O)_{str}$ and bending $(Z-O)_{bend}$ vibrations in ZO_4 tetrahedra ($2A_{1g} + 5E_g + T_{2g}$), four rotations of tetrahedra $(ZO_4)_{rot}$ ($1A_{1g} + 1E_g + 2T_{2g}$), four translations of tetrahedra $(ZO_4)_{trans}$ ($1E_g + 3T_{2g}$) and three vibrations involving a divalent *X*-site cation, especially Ca^{2+} ($1E_g + 2T_{2g}$). Vibrations of octahedrally coordinated *Y*-site cations are Raman inactive, therefore no direct information on the *Y*-site occupancy (mainly Zr, Ti, Al, Fe^{3+}) could be obtained (Kolesov and Geiger, 1998; Katerinopoulou *et al*., 2009).

Several well developed crystals of kerimasite were selected for detailed Raman spectroscopic study (Fig. 6; Table 3). Compared to common Ca-rich garnets, many Raman bands are shifted towards much lower frequencies, either due to Fe^{3+} substitution on the *Z* site (mainly among $(ZO_4)_{trans}$ and $(ZO_4)_{rot}$) or due to the strong influence of neighbouring octahedrally-coordinated Zr (Ti) cations on the internal vibrations of tetrahedra, that share oxygens. The detailed Raman spectra assignments are described and discussed in the Discussion section.

Associated garnets

Kerimasite commonly associates with other Ca garnets: andradite–grossular and their hydrated analogues. The andradite–grossular solid solution occurs as anhedral grains or aggregates, up to ~200 μm in size, which commonly form overgrowths on kerimasite (Fig. 2*b*–*c*). Andradite–grossular reveals irregular internal zoning due to variations in Fe and Al. The $^{Y}[Fe^{3+}/(Fe^{3+}+Al)]$ ratio shows wide variations (0.18 to 1.00). In some cases, tiny irregular Ti- and Zr-rich andradite zones were detected; they contain up

https://doi.org/10.1180/minmag.2015.079.3.15 Published online by Cambridge University Press

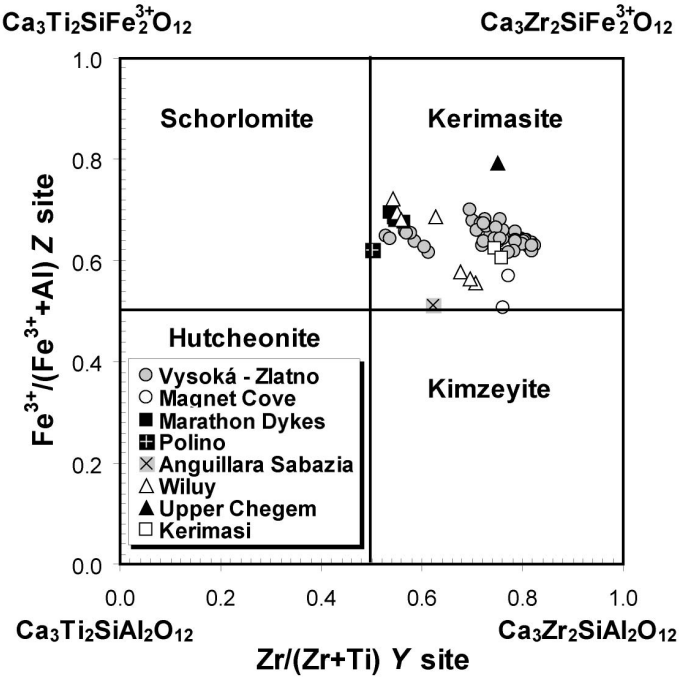

FIG. 3. $Fe^{3+}/(Fe^{3+} + Al)$ *Z* site *vs.* Zr/(Zr + Ti) *Y* site classification diagram (atomic proportions) of kerimasite from the Vysoká-Zlatno skarn in comparison with other known occurrences (compositions with $^{Z}Ti+^{Z}Fe^{2+} < 0.3$ a.p.f.u.; Platt and Mitchell, 1979; Lupini *et al.*, 1992; Schingaro *et al.*, 2001; Haynes *et al.*, 2003; Galuskin, 2005; Galuskina *et al.*, 2005, 2010*a*,*b*; Zaitsev *et al.*, 2010).

TABLE 3. The Raman wavenumbers of vibrational modes (cm^{-1}) and their attribution to bands and symmetry in kerimasite from the Vysoká-Zlatno skarn compared with data of Schingaro *et al*. (2001) and Zaitsev *et al*. (2010). Band labelling is after Pinet and Smith (1993).

Kerimasite	Bands — (this work) —	Attribution	Symmetry	Kimzeyite to kerimasite (Schingaro *et al.*, 2001)		Kerimasite (Zaitsev *et al.*, 2010)
987	I	$(Si-O)_{str}$	T_{2g}	–	–	–
877	II	$(Si-O)_{str}$	A_{1g}	–	–	875
843–845	III	$(Si-O)_{str}$	E_g+ T_{2g}	–	–	830
819–821	IV	$(Si-O)_{str}$	T_{2g}	–	–	–
782–783	IV	$(Fe^{3+}-O)_{str}$	T_{2g}	783	II, III, IV	785
731–732	II	$(Fe^{3+}-O)_{str}$	A_{1g}	730	II, III, IV	732
574–577	?V/VI	$(Z-O)_{bend}$	E_g/T_{2g}	–	–	573
503	VIII	$(Z-O)_{bend}$	E_g + T_{2g}	–	–	-
500–501	VII	$(Z-O)_{bend}$	A_{1g}	505	VII	500
412–414	IX	$(Z-O)_{bend}$	T_{2g}	424	not attributed	414
342–343	Xb	$(ZO_4)_{rot}$	A_{1g}	–	-	–
300–302	XI	$(ZO_4)_{rot}$	E_g	311	Xb	298
265–266	XIV	$(ZO_4)_{trans}$	T_{2g}	–	–	–
242–243	XV	X_{trans}	T_{2g}	253	not attributed	243
151–152	XVI	X_{trans}	E_g + T_{2g}	159	XVI	152

https://doi.org/10.1180/minmag.2015.079.3.15 Published online by Cambridge University Press

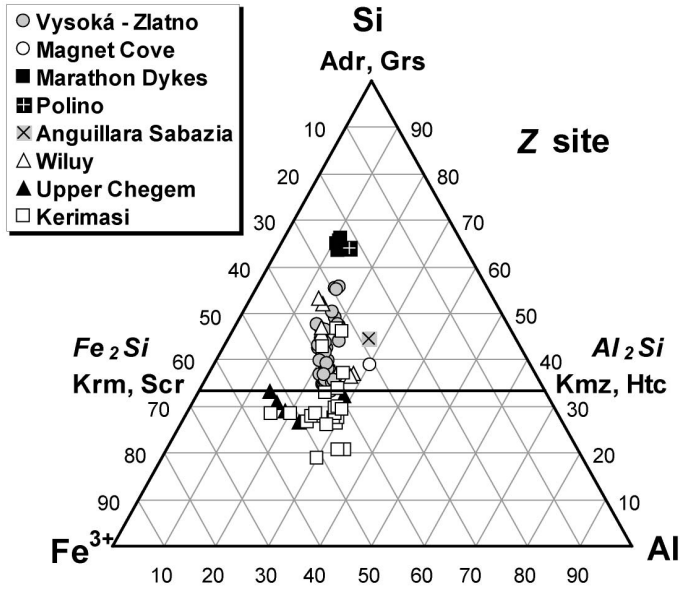

FIG. 4. Si–Fe^{3+}–Al *Z* site diagram (Zaitsev *et al.*, 2010, modified; atomic proportions, at.%) of kerimasite from the Vysoká-Zlatno skarn in comparison with other known occurrences [compositions with Si > ^{Z}(Ti, Fe^{2+}) and Si + ^{Z}Ti > 0.5 a.p.f.u.; Platt and Mitchell, 1979; Lupini *et al.*, 1992; Schingaro *et al.*, 2001; Haynes *et al.*, 2003; Galuskin, 2005; Galuskina *et al.*, 2005, 2010*a*,*b*,*d*; Zaitsev *et al.*, 2010]. The apex where Si = 100 at.% represents andradite (Adr) and grossular (Grs) end-members. The horizontal line at 33.3 at.% Si represents the end-member *Z*-site compostions of kerimasite (Krm), schorlomite (Scr) for Fe^{3+} > Al and kimzeyite (Kmz), hutcheonite (Htc) for Al > Fe^{3+}.

to 11 wt.% TiO_2 and ⩽4.4 wt.% ZrO_2 (Table 4). Smaller totals (~90 to 97 wt.%) and significant deviations from ideal stoichiometry based on anhydrous formulae (12 oxygen anions) indicate the presence of a hydroxyl anion in the structure of these garnets, also confirmed by micro-Raman spectroscopy. Internal vibrations of $(OH)^{-}$ anions are pronounced as a broad feature between 3500 and 3700 cm^{-1} (Fig. 7). Consequently, the formulae were normalized on the basis of three cations for the sum of the *X* site (Table 4). Some compositions of these hydroxyl-bearing garnets show significant deficiency of calculated Si (1.98 to 2.27 a.p.f.u.) and an absence, or lack, of calculated tetrahedral Al and Fe^{3+} (0.00 to 0.11 a.p.f.u.). Such formulae are close to holtstamite, [end-member formula: $Ca_3Al_2Si_2\square O_8(OH)_4$] or its Fe^{3+}-dominant, Ti,Zr-rich analogue [$Ca_3Fe^{3+}_2Si_2\square O_8(OH)_4$] with ^{Y}[$Fe^{3+}$/($Fe^{3+}$+Al)] = 0.90 (Table 4). However, without definite documentation of holtstamite, such as X-ray diffraction, these compositions are best referred to as hydrated grossular or hydrated andradite.

Discussion and conclusions

Crystal chemistry of kerimasite

Kerimasite and kimzeyite belong to garnets of the schorlomite group with principal Zr^{4+} cation occupancy in the *Y* site, and dominance of trivalent cations (M^{3+} = Fe^{3+}, Al) over Si^{4+} in the tetrahedral *Z* site. Kimzeyite compositions show Al>Fe^{3+}, whereas in kerimasite Fe^{3+}>Al, their end-member formulae are {Ca_3}[Zr_2]($SiAl_2$)O_{12} and {Ca_3}[Zr_2]($SiFe^{3+}_2$)O_{12}, respectively (Milton *et al.*, 1961; Zaitsev *et al.*, 2010; Grew *et al.*, 2013; Table 1).

The *X* site of the Vysoká-Zlatno kerimasite is filled almost exclusively by Ca^{2+} (2.988 to 3.086 a.p.f.u.); the same feature is characteristic of kerimasite–kimzeyite from all known occurrences: Wiluy River, Russia (Galuskin, 2005; Galuskina *et al.*, 2005, 2010*a*), Upper Chegem, Russia (Galuskina *et al.*, 2010*b*–*d*, 2013*a*,*b*), Magnet Cove, U.S.A. (Milton *et al.*, 1961; Lupini *et al.*, 1992; Haynes *et al.*, 2003), Stromboli, Italy (Munno *et al.*, 1980), Anguillara Sabazia, Italy (Schingaro *et al.*, 2001) and Kerimasi, Tanzania (Zaitsev *et al.*, 2010). A moderate surplus of Ca or

https://doi.org/10.1180/minmag.2015.079.3.15 Published online by Cambridge University Press

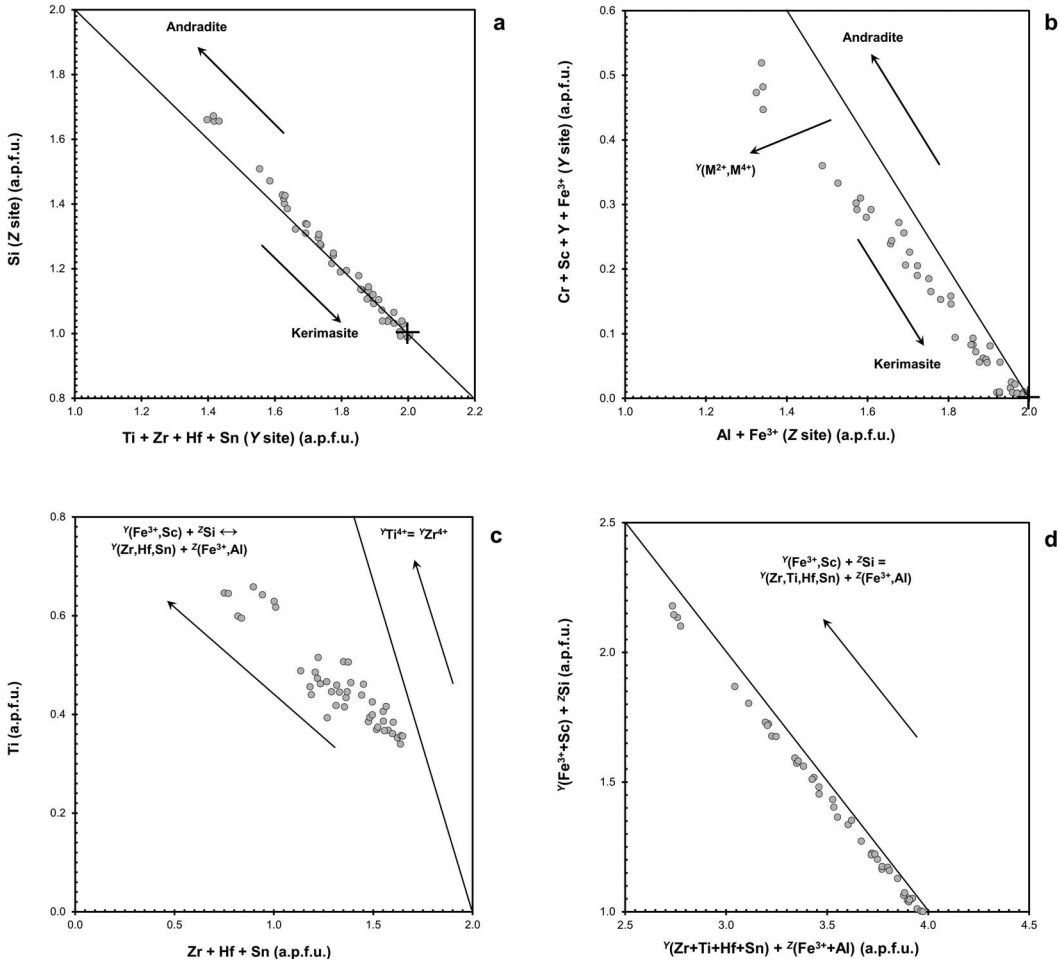

FIG. 5. Composition and substitution diagrams of kerimasite from the Vysoká-Zlatno skarn with position of the kerimasite end-member composition (+) in *a* and *b*: (*a*) Si (*Z* site) *vs.* Ti + Zr + Hf + Sn (M^{4+} cations in *Y* site); (*b*) Cr + Sc + Y + Fe^{3+} (M^{3+} cations in *Y* site) *vs.* Al + Fe^{3+} (M^{3+} cations in *Z* site); (*c*) Ti *vs.* Zr + Hf + Sn (M^{4+} cations in *Y* site); (*d*) $^{Y}(Fe^{3+} + Sc) + {}^{Z}Si$ *vs.* $^{Y}(Zr + Ti + Hf + Sn) + {}^{Z}(Fe^{3+} + Al)$.

an *X*-site content above theoretical value (~3.03 to 3.26 a.p.f.u.) is another specific phenomenon of kerimasite–kimzeyite solid solution, determined by both the classical wet and electron-microprobe analyses (Milton *et al.*, 1961; Lupini *et al.*, 1992; Schingaro *et al.*, 2001; Haynes *et al.*, 2003; Galuskina *et al.*, 2010*b*,*c*; Zaitsev *et al.*, 2010). However, the reason for this surplus in the *X* site and deviation from the ideal garnet stoichiometry is still not clear. It could be the result of a vacancy in the *Z* site which, calculated on an anion basis produces *X* site surplus. The vacancy could be charge-balanced by the presence of hydroxyl groups (Peters, 1965; Pasaglia and Rinaldi, 1984; Lager *et al.*, 1989; Galuskina and Galuskin, 2003; Galuskin, 2005) or by the substitution of cations with higher charge in neighbouring octahedral and tetrahedral sites. We can make some assumptions based on charge of sites after variable calculations of the formula. If we calculate the R1B41C analysis on the basis of 12 oxygen atoms, we get the formula with the largest *X*-site surplus of 3.056 a.p.f.u. (Table 2). The charge of the *X* site is 6.11, while the total charge of both octahedral and tetrahedral sites is 17.89. Therefore, there is a charge excess

https://doi.org/10.1180/minmag.2015.079.3.15 Published online by Cambridge University Press

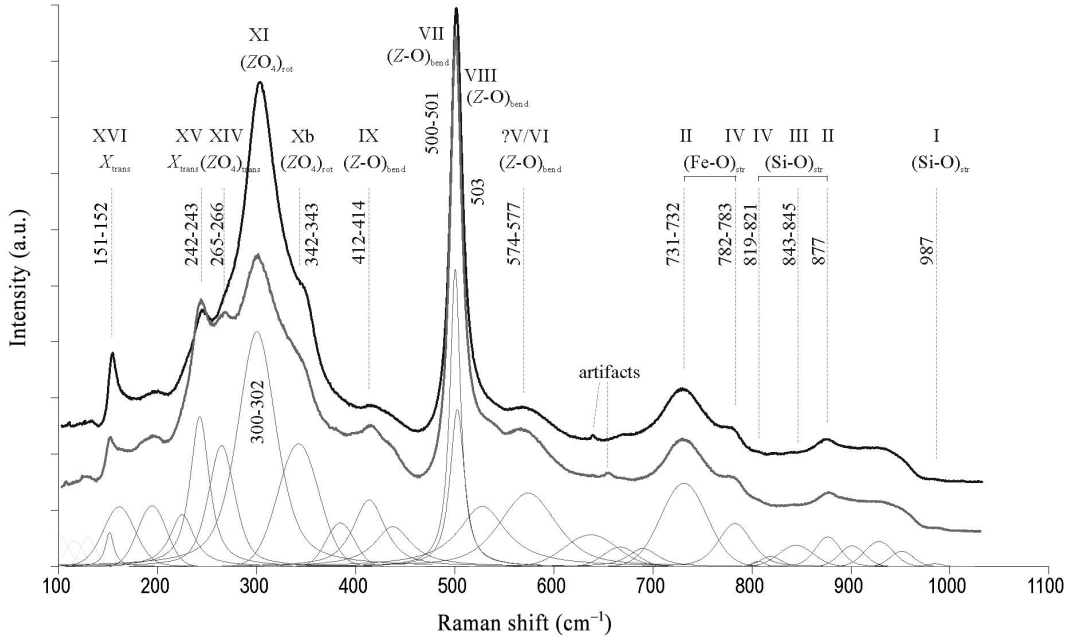

FIG. 6. Raman spectra of kerimasite from the Vysoká-Zlatno skarn recorded for two different crystal orientations.

in the *X* site and a charge deficiency in other sites. A similar charge ratio is also found in samples with smaller *X*-site surplus. The calculation on the basis of $X = 3$ a.p.f.u. gives the formula: $\{Ca_{2.997}Sr_{0.003}\}_{\Sigma 3.000}[Zr_{0.713}Ti_{0.634}Fe^{3+}_{0.585}Sc_{0.017}Hf_{0.016}Mg_{0.015}Sn_{0.009}Nb_{0.007}Mn_{0.003}Ta_{0.001}]_{\Sigma 2.000}$

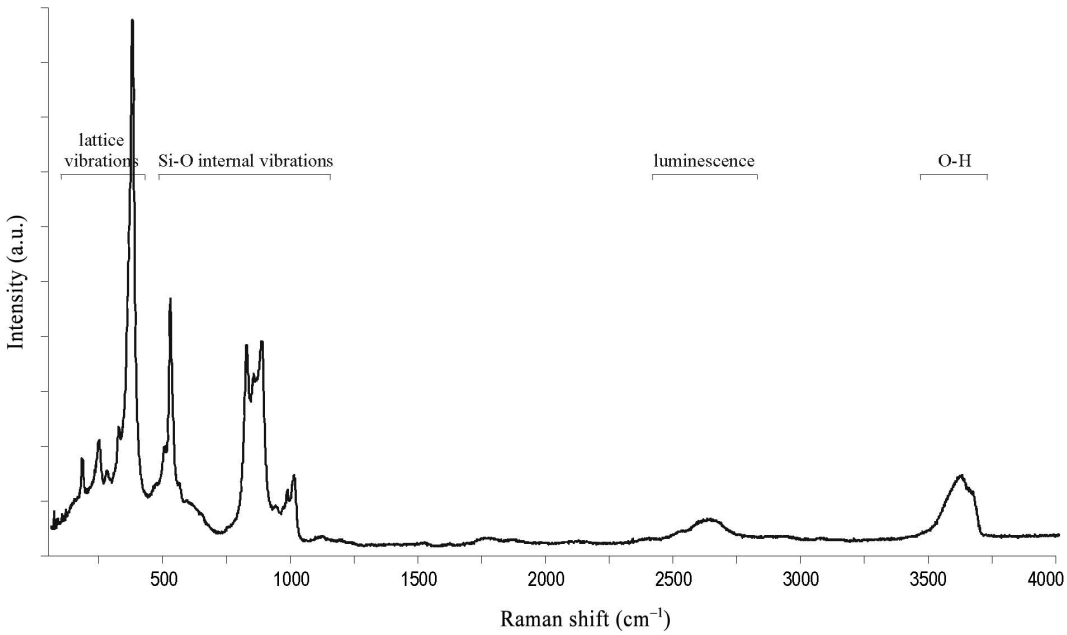

FIG. 7. Raman spectra of hydrated andradite from the Vysoká-Zlatno skarn.

https://doi.org/10.1180/minmag.2015.079.3.15 Published online by Cambridge University Press

TABLE 4. Representative electron-microprobe compositions (wt.%) of andradite, Ti,Zr-rich andradite (TiZr Adr), grossular and hydrated grossular and andradite from the Vysoká-Zlatno skarn.

Mineral	Andradite		TiZr Adr	Grossular	Hydrated grossular and andradite			
Sample #	R1A01	R1C17	R1B37C	R1A03	R1C18	R1C21	R1C22	R1B02E
P_2O_5	0.03	0.00	0.08	0.04	0.00	0.04	0.05	0.63
Nb_2O_5	0.00	0.00	0.14	0.00	0.00	0.00	0.00	0.18
SiO_2	32.78	29.47	23.61	32.52	27.70	29.39	30.04	24.38
TiO_2	0.73	0.94	11.00	0.15	0.03	0.05	0.04	6.96
ZrO_2	0.04	3.25	4.43	0.11	0.00	0.00	0.00	3.71
HfO_2	0.00	0.00	0.13	0.00	0.00	0.00	0.00	0.13
SnO_2	0.00	0.00	0.08	0.00	0.00	0.00	0.00	0.05
Al_2O_3	7.09	9.73	2.22	12.32	18.04	16.27	17.54	2.57
Cr_2O_3	0.00	0.00	0.08	0.00	0.00	0.00	0.00	0.09
Sc_2O_3	0.00	0.00	0.30	0.00	0.00	0.00	0.00	0.19
Fe_2O_3	20.87	17.21	24.23	14.40	6.21	8.43	7.03	20.69
MgO	0.00	0.00	0.00	0.00	0.07	0.00	0.00	0.00
CaO	35.02	34.92	33.74	36.11	37.42	37.35	37.18	34.48
Total	96.56	95.52	100.04	95.65	89.47	91.53	91.88	94.06
Formulae normalized on the basis of X = 3 a.p.f.u. and 12 anions								
P	0.002	0.000	0.006	0.003	0.000	0.003	0.003	0.043
Si	2.621	2.363	1.959	2.522	2.073	2.203	2.262	1.980
Al Z	0.000	0.142	0.217	0.000	0.000	0.000	0.000	0.113
Fe Z	0.000	0.000	0.416	0.000	0.000	0.000	0.000	0.000
Sum Z	2.623	2.505	2.598	2.525	2.073	2.206	2.265	2.136
Nb	0.000	0.000	0.005	0.000	0.000	0.000	0.000	0.007
Ti	0.044	0.057	0.686	0.009	0.002	0.003	0.002	0.425
Zr	0.002	0.127	0.179	0.004	0.000	0.000	0.000	0.147
Hf	0.000	0.000	0.003	0.000	0.000	0.000	0.000	0.003
Sn	0.000	0.000	0.003	0.000	0.000	0.000	0.000	0.002
Al	0.668	0.778	0.000	1.126	1.591	1.438	1.557	0.133
Cr	0.000	0.000	0.005	0.000	0.000	0.000	0.000	0.006
Sc	0.000	0.000	0.022	0.000	0.000	0.000	0.000	0.013
Fe	1.256	1.038	1.097	0.840	0.350	0.476	0.398	1.264
Mg	0.000	0.000	0.000	0.000	0.008	0.000	0.000	0.000
Sum Y	1.970	2.000	2.000	1.979	1.951	1.917	1.957	2.000
Ca X	3.000	3.000	3.000	3.000	3.000	3.000	3.000	3.000
Sum cations	7.592	7.505	7.599	7.503	7.023	7.122	7.223	7.136
O	10.450	10.062	10.646	10.053	8.139	8.581	8.936	9.065
OH	1.550	1.938	1.354	1.947	3.861	3.419	3.064	2.935
Sum anions	12.000	12.000	12.000	12.000	12.000	12.000	12.000	12.000
Cation charge	22.450	22.062	22.646	22.053	20.139	20.581	20.936	21.065
Anion charge	22.450	22.062	22.646	22.053	20.139	20.581	20.936	21.065
$^{Y}[Fe^{3+}/(Fe^{3+}+Al)]$	0.65	0.57	1.00	0.43	0.18	0.25	0.20	0.90

$(Si_{1.630}Fe^{3+}_{0.761}Al_{0.463}P_{0.002})_{\Sigma 2.856}O_{12}$. The charge of the X site is exactly 6.00 but the charge in other sites decreases even more, to 17.57. This contradicts the presumption of charge excess in the Y and Z sites and supports the hydroxylation of oxygens in the tetrahedral position. However, the largest calculated content of H_2O in kerimasite only reaches 0.24 wt.% and such a low

https://doi.org/10.1180/minmag.2015.079.3.15 Published online by Cambridge University Press

concentration was not detected by the micro-Raman spectroscopy (see the next section).

In the *Y* site, Zr^{4+} is the dominant cation of kerimasite. However, kerimasite compositions from described world localities show two basic compositional varieties (Fig. 8). (1) Ti-rich kerimasite contains larger amounts of Ti^{4+} (0.34 to 0.76 a.p.f.u.) and in some cases also Fe^{3+} (up to ~0.6 a.p.f.u.), but small to negligible amounts of other octahedral cations (mainly Sc^{3+}, Sn^{4+}, Sb^{5+}, Nb^{5+}, U^{6+}). Such compositions are typical for kerimasite from the investigated Vysoká-Zlatno skarn, the Magnet Cove carbonatite (Lupini *et al.*, 1992; Haynes *et al.*, 2003), carbonate-rich lamprophyre from Marathon Dikes, Ontario, Canada (Platt and Mitchell, 1979), Polino carbonatite, Italy (Lupini *et al.*, 1992), the Anguillara Sabazia melilite ejecta (Schingaro *et al.*, 2001), the Wiluy River rodingite skarn (Galuskin, 2005; Galuskina *et al.*, 2005, 2010*a*) and also occur rarely in the Upper Chegem caldera (Galuskina *et al.*, 2010*b*) and in the Kermasi carbonatite (Zaitsev *et al.*, 2010). (2) Ti-poor kerimasite compositions with Ti <0.26 a.p.f.u. and high concentrations of other octahedral cations (mainly Sc^{3+}, Sn^{4+}, Sb^{5+}, Nb^{5+}, U^{6+}). They represent solid solutions between the kerimasite end-member (or its Ti-analogue with Ti > Si in *Z* site) and newly discovered garnets from skarn xenoliths in the Upper Chegem Caldera: bitikleite, usturite, elbrusite, toturite, irinarassite and dzhuluite (Galuskina *et al.*, 2010*b*–*d*, 2013*a*,*b*). Moreover, kerimasite from its type locality (the Kerimasi carbonatite volcano and adjacent alluvial sediments), represents a Nb-rich variety with 0.04 to 0.48 Nb a.p.f.u. (Zaitsev *et al.*, 2010), towards the hypothetical $\{Ca_3\}[NbZr](Fe_3^{3+})O_{12}$ end-member.

Kerimasite, as a Zr-rich mineral, usually includes some hafnium, an element with high geochemical affinity to Zr. Measured Hf concentrations in the Vysoká-Zlatno kerimasite reach the largest values of this element ever reported in this mineral: 0.4 to 1.7 wt.% HfO_2, 0.01 to 0.05 a.p.f.u. (Table 2; Fig. 9). Published Hf contents range from ~0.1 to 0.8 wt.% HfO_2, up to 0.02 a.p.f.u. (Galuskin, 2005; Galuskina *et al.*,

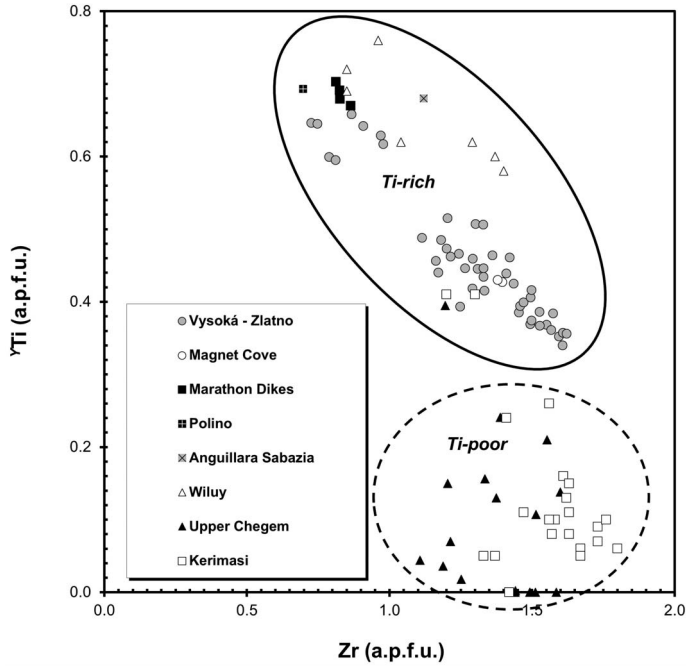

FIG. 8. ^{Y}Ti *vs.* Zr compositional diagram (atomic proportions) of kerimasite from the Vysoká-Zlatno skarn in comparison with other known occurrences (Platt and Mitchell, 1979; Lupini *et al.*, 1992; Schingaro *et al.*, 2001; Haynes *et al.*, 2003; Galuskin, 2005; Galuskina *et al.*, 2005, 2010*a*–*d*, 2013*a*,*b*; Zaitsev *et al.*, 2010) showing Ti-rich and Ti-poor kerimasite compositions.

https://doi.org/10.1180/minmag.2015.079.3.15 Published online by Cambridge University Press

2005, 2010*a*–*d*; 2013*a*,*b*; Zaitsev *et al.*, 2010). A near end-member hafniun analogue of kerimasite ($Ca_3Hf_2Fe_2SiO_{12}$) and hafnian kerimasite–kimzeyite intermediate composition ($Ca_3Hf_2FeAlSiO_{12}$) have been synthesized (Whittle *et al.*, 2007). The average Zr/Hf weight ratio of the kerimasite investigated is 33.3, a value consistent with the continental crust (e.g. Taylor and McLennan, 1985).

The kerimasite formula in an ideal kerimasite–kimzeyite solid solution shows atomic Fe^{3+} > Al and (Fe^{3+},Al) > Si relations in the tetrahedral *Z*-site position. The $^{Z}[Fe^{3+}/(Fe^{3+}+Al)]$ ratio is 0.61 to 0.70 in the samples investigated and these values fit into the range for other reported kerimasite compositions (0.50 to 0.82; Lupini *et al.*, 1992; Schingaro *et al.*, 2001; Haynes *et al.*, 2003; Galuskin, 2005; Galuskina *et al.*, 2005, 2010*a*–*d*, 2013*a*,*b*; Zaitsev *et al.*, 2010). However, crystal-chemical formulae of Sn-, Sb- and U-rich and ^{Y}Ti-poor kerimasites from the Upper Chegem skarn xenoliths indicate an important presence of Ti^{4+} (up to 0.54 a.p.f.u.) and Fe^{2+} (up to 0.33 a.p.f.u.) in the tetrahedral *Z* site, in some cases with ^{Z}Ti > Si or $^{Z}Fe^{2+}$ > Si (Galuskina *et al.*, 2010*b*–*d*, 2013*a*,*b*).

Micro-Raman spectroscopy of kerimasite

The assignment and interpretation of kerimasite Raman spectra (Fig. 6, Table 3) is based on spectroscopic data for uvarovite–grossular–andradite garnets (UGA) of Pinet and Smith (1993), adopting their peak labelling (I to XVI) and symmetry, kerimasite and related Ca,Zr,Ti-rich garnet members (Schingaro *et al.*, 2001; Katerinopoulou *et al.*, 2009; Zaitsev *et al.*, 2010; Galuskina *et al.*, 2005, 2010*a*–*d*, 2013*a*,*b*) and comparison of data for uvarovite (Chopelas, 2005) and other silicate garnets (Kolesov and Geiger, 1998). The absence of internal vibrations in the region between ~3300 and 3700 cm^{-1} show negligible (if any) $(OH)^{-}$ anion content in the kerimasite studied.

(I–IV): Raman peaks in spectral region ~700–1000 cm^{-1} represent symmetric stretching vibrations in (Z–O_4) tetrahedra. The 819–821 to 987 cm^{-1} bands indicate the presence of $(SiO_4)^{4-}$ tetrahedra, whereas 731–732 and 782–783 cm^{-1} bands are typical for symmetric Fe^{3+}–O (and/or Al–O) stretching vibrations of $[(Fe^{3+},Al)O_4]^{5-}$ tetrahedra (Schingaro *et al.*, 2001; Katerinopoluou *et al.*, 2009; Galuskina *et al.*, 2010*b*–*d*, 2013*a*,*b*).

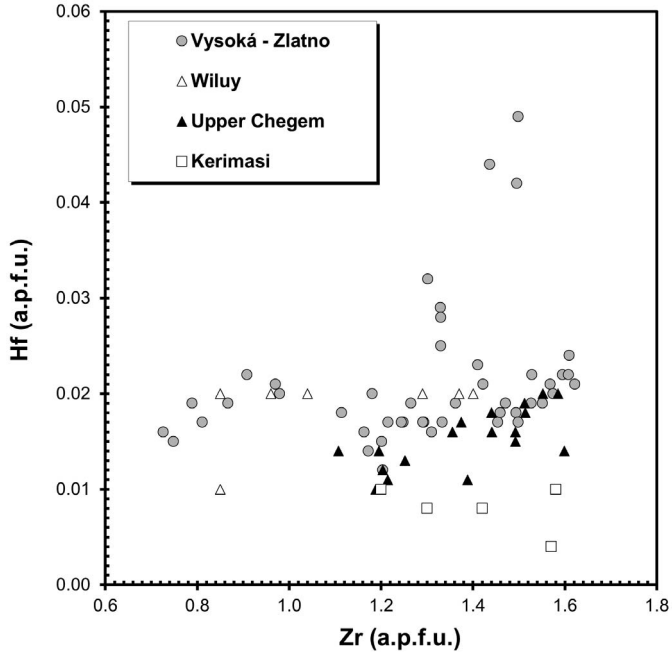

FIG. 9. Hf *vs.* Zr compositional diagram (atomic proportions) of kerimasite from the Vysoká-Zlatno skarn in comparison with other known occurrences (Galuskin, 2005; Galuskina *et al.*, 2005, 2010*a*–*d*, 2013*a*,*b*; Zaitsev *et al.*, 2010).

https://doi.org/10.1180/minmag.2015.079.3.15 Published online by Cambridge University Press

(?V/VI): In the Pinet and Smith (1993) dataset, both of these bands display strong dependence on the *Y*-site cation. In the Al–Cr–Fe sequence, the wavenumber of the (V) band decreases with increasing atomic number, while in the (VI) band the downshift is counterbalanced by the opposite effect of ionic radius. Extrapolation to the Zr^{4+} cation would probably shift the (V) band to a much lower wavenumber, while that of (VI) band should increase. Despite the unknown effect of charge at the *Y* site and of Fe^{3+} substitution at the *Z* site, 574–577 cm^{-1} has been labelled tentatively as either (V) or (VI) internal mode.

(VII–VIII): In UGA garnets (VII) remains a single band with a wavenumber depending on the *Y*-site cation, while (VIII) splits into separate bands specific for particular substituents. Yet the convergence of these two peaks in andradite implies that they may merge in kerimasite to form one dominant (VII) band at 500–501 cm^{-1}.

(IX): The 412–414 cm^{-1} (*Z*–O) band is subject to a similar *Y*-site dependent shift as in (V) due to the effect of octahedral Zr^{4+} on shared oxygen.

(X): The shoulder at 342–343 cm^{-1} is not clearly identified. Its intensity is nearly invariant to the polarization direction, pointing to the (Xb) band with A_{1g} symmetry.

(XI): The distinctive band at 300–302 cm^{-1} was previously assigned to the (Xb) vibration with A_{1g} symmetry (Shingaro *et al.*, 2001; Galuskina *et al.*, 2013*a*). However, due to strong variations with orientation, we suggest an anisotropic mode, probably the (XI) peak (E_g mode). It usually dominates this spectral region in all garnet species, in contrast to (Xb), that usually appears as a weak shoulder (Pinet and Smith, 1993). Chopelas (2005) attributes the dominance of E_g modes over A_{1g} in this spectral region to magnetic properties of transition metals in the *Y* position.

(XIV): This mode, unique to UGA garnets (Pinet and Smith, 1993), is assigned to translation of tetrahedra [$(ZO_4)_{trans}$]. In kerimasite it may be split into a $(SiO_4)^{4-}$ component at 265–266 cm^{-1} and Fe^{3+}/Al-substituted components, vibrating at lower wavenumbers.

(XV–XVI): Bands at 242–243 and 151–152 cm^{-1} appear in ranges typical of vibrations involving divalent cations (Ca^{2+}) at dodecahedrally coordinated *X*-site positions (Pinet and Smith, 1993; Schingaro *et al.*, 2001; Galuskina *et al.*, 2010*b*,*c*, 2013*a*,*b*). The former fits the translation T_{2g} mode of uvarovite (Chopelas, 2005). In oriented measurements, the peak at 151–152 cm^{-1} varies in concert with the E_g mode at 300–302 cm^{-1} (XI), thus it may represent the E_g component of the (XVI) mode.

However, for further improvement of these assignments a polarization study on oriented kerimasite crystals would need to be undertaken.

Genetic conditions of kerimasite formation

The textural relationships of the investigated skarn sample (R-1/677) indicate a high-grade, peak contact-metamorphic assemblage of kerimasite with monticellite, perovskite, spinel and Mg-rich magnetite, whereas andradite, grossular, clintonite, calcite, hydroxylellestadite–fluorellestadite, anhydrite and rare celestine show texturally younger positions and probably belong to a retrograde metamorphic association. Brucite, hydrotalcite, clinochlore and valeriite represent the youngest, relatively low-temperature assemblage. Scarce sulfide minerals (pyrrhotite, cobaltpentlandite, chalcopyrite, sphalerite, galena) probably precipitated in various genetic stages, from high-temperature contact metamorphism to low-temperature hydrothermal overprint.

The backscatter electron images of kerimasite crystals reveal two principal textural patterns due to Zr, Ti, Fe and Al variations. The regular, oscillatory concentric zoning (Fig. 2*d,e*) indicate a primary growth of kerimasite during the peak stage of the contact metamorphism, whereas irregular patchy internal textures (Fig. 2*f*) indicate partial alteration and dissolution-reprecipitation of kerimasite as well as its partial replacement by younger garnets (mainly andradite) during the retrograde phase (Fig. 2*b–c*).

The presence of kerimasite, monticellite, perovskite and other associated minerals indicate a relatively Ca-rich and Si-poor (SiO_2 undersaturated) environment during the contact metamorphic event. A primary source of zirconium in the skarn is not clear; both clastic zircon from the Triassic sediments or Zr input from intruded granodiorite/diorite magma could be possible sources. The Si-poor environment reflects the primary lithology of the sedimentary protolith of the Vysoká-Zlatno skarn, represented by the Upper Triassic sequence of marl slates with widespread limestone, dolomite, anhydrite and gypsum beds, which was favourable to precipitation of kerimasite, perovskite and other Si-deficient minerals during the metamorphic overprint (Fig. 10). Conversely, increased activity of SiO_2 (or H_4SiO_4) led to breakdown of kerimasite–

https://doi.org/10.1180/minmag.2015.079.3.15 Published online by Cambridge University Press

kimzeyite and perovskite to andradite–grossular, zircon and titanite:

$$Ca_3Zr_2(Fe,Al)_2SiO_{12} + CaTiO_3 + 5SiO_2 = Ca_3(Fe,Al)_2Si_3O_{12} + 2ZrSiO_4 + CaTiSiO_5$$

Analogous mineral assemblages, commonly including Ca-Zr-(Ti) garnets (kerimasite, kimzeyite, Zr-rich schorlomite), baddeleyite (ZrO_2) and/or other Ca-Zr-(Ti) oxide and silicate minerals (zirkelite, tazheranite, zirconolite, calzirite, baghdadite) as well as monticellite, perovskite and other Ca-rich phases, are characteristic for other calcic skarns and Ca-rich xenoliths in volcanic rocks worldwide (e.g. Al-Hermezi *et al.*, 1986; Williams and Gieré, 1988; Jamtveit *et al.*, 1997; Pascal *et al.*, 2001; Wenzel *et al.*, 2002; Galuskin, 2005; Galuskina *et al.*, 2005, 2010*a*–*d*, 2013*a*,*b*).

A complete solid solution between synthetic kerimasite ($Ca_3Zr_2Fe_2SiO_{12}$) and kimzeyite ($Ca_3Zr_2Al_2SiO_{12}$) end-members was prepared at a temperature of 680ºC and pressure of 200 MPa (2000 atm.), whereas $Ca_3Zr_2Fe_2SiO_{12}$ melts at 1290±10ºC in air (Ito and Frondel, 1967). A solid solution between kerimasite and a kerimasite–kimzeyite intermediate member (1:1) were synthesized at temperatures of 550 to 700ºC and 100 MPa (1000 kg/cm^2) pressure, but runs <550ºC were not succesful (Yamakawa *et al.*, 1993). However, Whittle *et al.* (2007) synthesized kerimasite, kerimasite–kimzeyite and their Hf analogues at a distinctly higher temperature of 1400ºC.

Estimated temperatures for the formation of kerimasite and associated garnets is during high-temperature and low-pressure contact metamorphism exceeding 800ºC for Wiluy rodingite-like rocks (Galuskin, 2005; Galuskina *et al.*, 2005, 2010*a*) or in the range 800–1000ºC for skarn xenoliths of the Upper Chegem Caldera (Galuskina *et al.*, 2010*b*,*c*, 2013*a*). The *P-T*

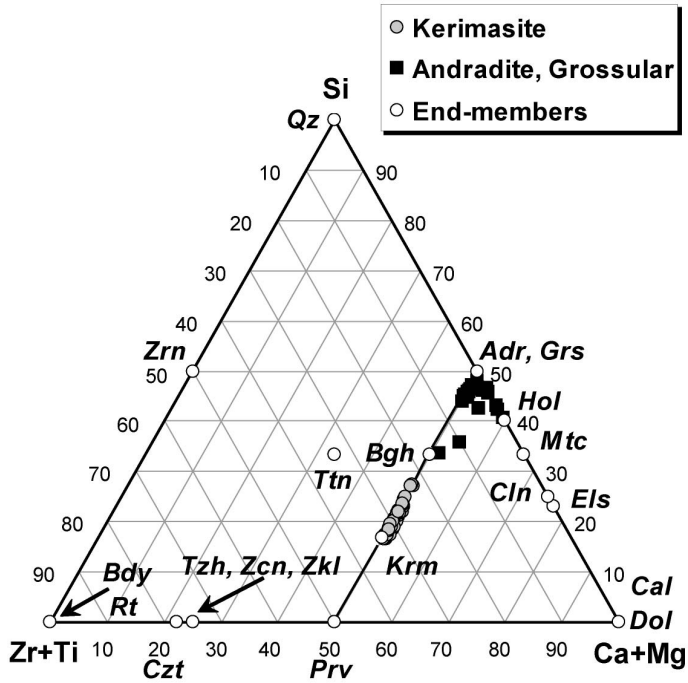

FIG. 10. Triangular Si – Zr+Ti – Ca+Mg phase diagram (atomic proportions) of characteristic Ca-silicate and Zr(Ti)-bearing minerals in calcic skarns and quartz (end-member formulae) in comparison with compositions of kerimasite, andradite and grossular (including hydrated compositions) from the Vysoká-Zlatno skarn. Mineral abbreviations: Qz – quartz; Zrn – zircon; Bdy – baddeleyite; Rt – rutile; Czt – calzirtite; Tzh – tazheranite; Zcn – zirconolite; Zkl – zirkelite, Prv – perovskite; Cal – calcite; Dol – dolomite; Krm – kerimasite (kimzeyite, schorlomite); Ttn – titanite; Bgh – baghdadite; Els – ellestadite; Cln – clintonite; Mtc – monticellite; Hol – holtstamite; Adr – andradite; Grs – grossular.

https://doi.org/10.1180/minmag.2015.079.3.15 Published online by Cambridge University Press

parameters of the peak-stage contact-metamorphic association from the Vysoká-Zlatno skarn with monticellite, kerimasite, perovskite and spinel could be compared with analogous Ca-Mg skarn assemblages. Monticellite represents a typical olivine-group mineral of high-temperature skarns; it forms by breakdown of Ca- and Mg-rich phases, especially forsterite, diopside and calcite (e.g. Walter 1963*a*,*b*; Tracy *et al.*, 1978; Deer *et al.*, 1997; Galuskin *et al.*, 2005). The upper thermal stability and breakdown of monticellite is constrained by several reactions with production of åkermanite, merwinite, periclase and forsterite. The reactions indicate the temperature stability field of the monticellite-bearing assemblages are roughly between T ~550 and ~900ºC at $P \leqslant 200$ MPa (2 kbar) and $X(CO_2) \geqslant 0.1$ (Deer *et al.*, 1997; Galuskin, 2005, and references therein).

Moreover, the maximum temperature of the Vysoká-Zlatno skarn could be estimated on a final eutectic crystallization of adjacent granodiorite porphyry groudmass, based on two-feldspar and Fe-Ti oxide geothermometry, which gives 700 to 720ºC (Konečný, 2002). The probable pressure range results from an assumed emplacement depth of the porphyry intrusion in the central zone of the Štiavnica stratovolcano (~1.2 to 1.8 km), based on paleovolcanic reconstruction (Lexa *et al.*, 1999). Consequently, precipitation of the peak-stage contact-metamorphic minerals of the Vysoká-Zlatno skarn including kerimasite and monticellite could be approximated at T ~700ºC and P ~50 to 70 MPa (0.5–0.7 kbar).

Acknowledgements

This work was supported by the Slovak Research and Development Agency under the contracts No. APVV-0537-10, APVV-0081-10, VEGA 1/0257/13 and VEGA 1/0560/15. The authors thank Patrik Konečný and Daniel Ozdín for assistance during electron-microprobe measurements. They are grateful to A. Zaitsev, one anonymous reviewer and the Associate Editor, E. Grew, whose critical and constructive comments and discussion improved this work significantly.

References

Al-Hermezi, McKie, D. and Hall, A.J. (1986) Baghdadite, a new calcium zirconium silicate mineral from Iraq. *Mineralogical Magazine*, **50**, 119–123.

Aroyo, M.I., Perez-Mato, J.M., Capillas, C., Kroumova, E., Ivantchev, S., Madariaga, G., Kirov, A. and Wondratschek, H. (2006*a*) Bilbao Crystallographic Server I: Databases and crystallographic computing programs. *Zeitschrift für Kristallographie*, **221**, 15–27.

Aroyo, M.I., Kirov, A., Capillas, C., Perez-Mato, J.M. and Wondratschek, H. (2006*b*) Bilbao Crystallographic Server II: Representations of crystallographic point groups and space groups. *Acta Crystallographica*, **A62**, 115–128.

Aroyo, M.I., Perez-Mato, J.M., Orobengoa, D., Tasci, E., de la Flor, G. and Kirov, A. (2011) Crystallography online: Bilbao Crystallographic Server. *Bulgarian Chemical Communications*, **43**, 183–197.

Burian, J. and Smolka, J. (1982) Geology of the porphyry copper deposit Zlatno. *Mineralia Slovaca*, **14**, 517–538 [in Slovak].

Chakhmouradian, A.R. and McCammon, C.A. (2005) Schorlomite: a discussion of the crystal chemistry, formula, and inter-species boundaries. *Physics and Chemistry of Minerals*, **32**, 277–289.

Chernyshev, I.V., Konečný, V., Lexa, J., Kovalenker, V.A., Jeleň, S., Lebedev, V.A. and Goltsman, Y.V. (2013) K-Ar and Rb-Sr geochronology and evolution of the Štiavnica Stratovolcano (Central Slovakia). *Geologica Carpathica*, **64**, 327–351.

Chopelas, A. (2005) Single crystal Raman spectrum of uvarovite, $Ca_3Cr_2Si_3O_{12}$. *Physics and Chemistry of Minerals*, **32**, 525–530.

Deer, W.A., Howie, R.A. and Zussman, J. (1997) *Rock-forming minerals. Vol. 1A Orthosilicates*. 2nd edition. The Geological Society, London, pp. 919.

Downs, R.T. and Hall-Wallace, M. (2003) The American Mineralogist crystal structure database. *American Mineralogist*, **88**, 247–250.

Galuskin, E. (2005) *Minerals of the Vesuvianite Group from the Achtarandite Rocks (Wiluy River, Yakutia)*. University of Silesia Publishing House, Katowice, Poland, pp. 192 [in Polish].

Galuskina, I.O. and Galuskin, E.V. (2003) Garnets of the hydrogrossular – ''hydroandradite" – ''hydroschorlomite" series. *Special Papers of the Mineralogical Society of Poland*, **22**, 54–57.

Galuskina, I.O., Galuskin, E.V., Dzierzanowski, P., Armbruster, T. and Kozanecki, M. (2005) A natural scandian garnet. *American Mineralogist*, **90**, 1688–1692.

Galuskina, I.O., Galuskin, E.V., Lazic, B., Armbruster, T., Dzierżanowski, P., Prusik, K. and Wrzalik, R. (2010*a*) Eringaite, $Ca_3Sc_2(SiO_4)_3$, a new mineral of the garnet group. *Mineralogical Magazine*, **74**, 365–373.

Galuskina, I.O., Galuskin, E.V., Armbruster, T., Lazic, B., Dzierżanowski, P., Gazeev, V.M., Prusik, K., Pertsev, N.N., Winiarski, A., Zadov, A.E., Wrzalik,

https://doi.org/10.1180/minmag.2015.079.3.15 Published online by Cambridge University Press

R. and Gurbanov, A.G. (2010*b*) Bitikleite-(SnAl) and bitikleite-(ZrFe): new garnets from xenoliths of the Upper Chegem volcanic structure, Kabardino-Balkaria, Northern Caucasus, Russia. *American Mineralogist*, **95**, 959–967.

Galuskina, I.O., Galuskin, E.V., Armbruster, T., Lazic, B., Kusz, J., Dzierżanowski, P., Gazeev, V.M., Pertsev, N.N., Prusik, K., Zadov, A.E., Winiarski, A., Wrzalik, R. and Gurbanov, A.E. (2010*c*) Elbrusite-(Zr) – a new uranian garnet from the Upper Chegem Caldera, Kabardino-Balkaria, Northern Caucasus, Russia. *American Mineralogist*, **95**, 1172–1181.

Galuskina, I.O., Galuskin, E.V., Dzierżanowski, P., Gazeev, V.M., Prusik, K., Pertsev, N.N., Winiarski, A., Zadov, A.E. and Wrzalik, R. (2010*d*) Toturite $Ca_3Sn_2Fe_2SiO_{12}$ – a new mineral species of the garnet group. *American Mineralogist*, **95**, 1305–1311.

Galuskina, I.O., Galuskin, E.V., Prusik, K., Gazeev, V.M., Pertsev, N.N. and Dzierżanowski, P. (2013*a*) Irinarassite $Ca_3Sn_2SiAl_2O_{12}$ – new garnet from the Upper Chegem Caldera, Northern Caucasus, Kabardino-Balkaria, Russia. *Mineralogical Maazine*, **77**, 2857–2866.

Galuskina, I.O., Galuskin, E.V., Kusz, J., Dzierżanowski, P., Prusik, K., Gazeev, V.M., Pertsev, N.N. and Dubrovinsky, L. (2013*b*) Dzhuluite, $Ca_3SbSnFe_3^{3+}O_{12}$, a new bitikleite-group garnet from the Upper Chegem Caldera, Northern Caucasus, Kabardino-Balkaria, Russia. *European Journal of Mineralogy*, **25**, 231–239.

Grew, E.S., Locock, A.J., Mills, S.J., Galuskina, I.O., Galuskin, E.V. and Hålenius, U. (2013) Nomenclature of the garnet supergroup. *American Mineralogist*, **98**, 785–811.

Gwalani, L.G., Rock, N.M.S., Ramasamy, R., Griffin, B.J. and Mulai, B.P. (2000) Complexly zoned Ti-rich melanite-schorlomite garnets from Ambadungar carbonatite-alkalic complex, Deccan Igneous Province, Gujarat State, Western India. *Journal of Asian Earth Sciences*, **18**, 163–176.

Haynes, E.A., Moecher, D.P. and Spicuzza, M.J. (2003) Oxygen isotope composition of carbonates, silicates, and oxides in selected carbonatites: constraints on crystallization temperatures of carbonatite magmas. *Chemical Geology*, **193**, 43–57.

Ito, J. and Frondel, C. (1967) Synthetic zirconium and titanium garnets. *American Mineralogist*, **52**, 773–781.

Jamtveit, B., Dahlgren, S. and Austrheim, H. (1997) High-grade contact metamorphism of calcareous rocks from the Oslo Rift, Southern Norway. *American Mineralogist*, **82**, 1241–1254.

Katerinopoulou, A., Katerinopoulos, A., Voudouris, P., Bieniok, A., Musso, M. and Amthauer, G. (2009) A multi-analytical study of the crystal structure of unusual Ti-Zr-Cr-rich andradite from the Maronia skarn, Rhodope massif, western Thrace, Greece. *Mineralogy and Petrology*, **95**, 113–124.

Koděra, P., Uher, P., Ozdín, D., Kollárová, V. and Lexa, J. (2009) Monticellite, clintonite and hydroxylellestadite-fluorellestadite: rare skarn minerals from the Vysoká-Zlatno Cu-Au skarn-porphyry deposit (Štiavnica stratovolcano). *Mineralia Slovaca*, **41**, 169–178 [in Slovak].

Koděra, P., Lexa, J. and Fallick, A.E. (2010) Formation of the Vysoká-Zlatno Cu-Au skarn-porphyry deposit, Slovakia. *Mineralium Deposita*, **45**, 817–843.

Kohút, M. and Danišík, M. (2013) Geochronometry of the granitic rocks from the Central Slovakian Neovolcanic Field – an evidence for rapid uplift. Pp. 25–26 in: *Geological Evolution of the Western Carpathians: New Ideas in the Field of Interregional Correlations* (I. Broska and A. Tomašových (editors). Abstract book. Geological Institute, Slovak Academy of Sciences, Bratislava.

Kolesov, B.A. and Geiger, C.A. (1998) Raman spectra of silicate garnets. *Physics and Chemistry of Minerals*, **25**, 142–151.

Konečný, P. (2002) *Evolution of magmatic reservoir underneath the Štiavnica stratovolcano*. Unpublished PhD thesis, Comenius University, Bratislava, pp. 273 [in Slovak].

Koritnig, S., Rösch, H., Schneider, A. and Seifert, F. (1978) The titanium-zirconium garnet of calc-silicate rock inclusions of the gabbro of Radautal, Harz Mountains, F. R. Germany. *Tschermak's Mineralogische und Petrographische Mitteilungen*, **25**, 305–313 [in German].

Kroumova, E., Aroyo, M.I., Perez-Mato, J.M., Kirov, A., Capillas, C., Ivantchev, S. and Wondratschek, H. (2003) Bilbao Crystallographic Server: useful databases and tools for phase transitions studies. *Phase Transitions*, **76**, 155–170.

Lager, G.A., Armbruster, T., Rotella, F.J. and Rossman, G.R. (1989) OH substitution in garnets: X-ray and neutron diffraction, infrared, and geometric-modeling studies. *American Mineralogist*, **74**, 840–851.

Lexa, J., Štohl, J. and Konečný, V. (1999) Banská Štiavnica ore district: relationship among metallogenetic processes and geological evolution of the central volcanic zone. *Mineralium Deposita*, **34**, 639–654.

Lupini, L., Williams, C.T. and Woolley, A.R. (1992) Zr-rich garnet and Zr- and Th-rich perovskite from the Polino carbonatite, Italy. *Mineralogical Magazine*, **56**, 581–586.

Ma, C. and Krot, A.N. (2014) Hutcheonite, $Ca_3Ti_2(SiAl_2)O_{12}$, a new garnet mineral from the Allende meteorite: an alteration phase in a Ca-Al-rich inclusion. *American Mineralogist*, **99**, 667–670.

https://doi.org/10.1180/minmag.2015.079.3.15 Published online by Cambridge University Press

Milton, C., Ingram, B.L. and Blade, L.V. (1961) Kimzeyite, a zirconium garnet from Magnet Cove, Arkansas. *American Mineralogist*, **46**, 533–548.

Munno, R., Rossi, G. and Tadini, C. (1980) Crystal chemistry of kimzeyite from Stromboli, Aeolian Islands, Italy. *American Mineralogist*, **65**, 188–191.

Pascal, M.-L., Fonteilles, M., Verkaeren, J., Piret, R. and Marincea, Ş. (2001) The melilite-bearing high-temperature skarns of the Apuseni Mountains, Carpathians, Romania. *The Canadian Mineralogist*, **39**, 1405–1434.

Passaglia, E. and Rinaldi, R. (1984) Katoite, a new member of the $Ca_3Al_2(SiO_4)_3$–$Ca_3Al_2(OH)_{12}$ series and a new nomenclature for the hydrogrossular group of minerals. *Bulletin de la Société Française de Minéralogie et de Cristallographie*, **107**, 605–618.

Peters, T. (1965) A water-bearing andradite from the Totalp serpentine (Davos, Switzerland). *American Mineralogist*, **50**, 1482–1486.

Pinet, M. and Smith, D.C. (1993) Raman microspectrometry of garnets $X_3Y_2Z_3O_{12}$: I. Natural calcian uvarovite-grossular-andradite series. *Schweizerische Mineralogische und Petrographische Mitteilungen*, **73**, 21–40 [in French].

Platt, R.G. and Mitchell, R.H. (1979) The Marathon Dikes. I: Zirconium-rich titanian garnets and manganoan magnesian ulvöspinel–magnetite spinels. *American Mineralogist*, **64**, 546–550.

Pouchou, J.L. and Pichoir, F. (1985) 'PAP' (φ ρZ) procedure for improved quantitative microanalysis. Pp. 104–106 in: *Microbeam Analysis* (J.T. Armstrong, editor). San Francisco Press, San Francisco, USA.

Schingaro, E., Scordari, F., Capitanio, F., Parodi, G., Smith, D.C. and Mottana, A. (2001) Crystal chemistry of kimzeyite from Anguillara, Mts. Sabatini, Italy. *European Journal of Mineralogy*, **13**, 749–759.

Taylor, S.R. and McLennan, S.M. (1985) *The Continental Crust: its Composition and Evolution*. Blackwell, Oxford, pp. 312.

Tracy, R.J., Jaffe, H.W. and Robinson, P. (1978) Monticellite marble at Cascade Mountain, Adirondack Mountains, New York. *American Mineralogist*, **63**, 991–999.

Uher, P., Koděra, P. and Vaculovič, T. (2011) Perovskite from Ca-Mg skarn-porphyry deposit Vysoká – Zlatno, Štiavnica stratovolcano, Slovakia. *Mineralia Slovaca*, **43**, 247–254.

Ulrych, J., Povondra, P., Pivec, E., Rutšek, J. and Sitek, J. (1994) Compositional evolution of metasomatic garnet in melilitic rocks of the Osečná Complex, Bohemia. *The Canadian Mineralogist*, **32**, 637–647.

Walter, L.S. (1963*a*) Experimental studies on Bowen's decarbonization series. I: P-T univariant equilibria of the 'monticellite' and 'akermanite' reactions. *American Journal of Science*, **261**, 488–500.

Walter, L.S. (1963*b*) Experimental studies on Bowen's decarbonization series. II: P-T univariant equilibria of reaction forsterite + calcite = monticellite + periclase + CO_2. *American Journal of Science*, **261**, 773–779.

Wenzel, T., Baumgartner, L.P., Brügmann, G.E., Konnikov, E.G. and Kislov, E.V. (2002) Partial melting and assimilation of dolomitic xenoliths by mafic magma: the Ioko-Dovyren intrusion (North Baikal Region, Russia). *Journal of Petrology*, **43**, 2049–2074.

Whittle, K.R., Lumpkin, G.R., Berry, F.J., Oates, G., Smith, K.L., Yudintsev, S. and Zaluzec, N.J. (2007) The structure and ordering of zirconium and hafnium containing garnets studied by electron channelling, neutron diffraction and Mössbauer spectroscopy. *Journal of Solid State Chemistry*, **180**, 785–791.

Williams, C.T. and Gieré, R. (1988) Metasomatic zonation of REE in zirconolite from a marble skarn at the Bergell contact aureole (Switzerland/Italy). *Schweizerische Mineralogische und Petrographische Mitteilungen*, **68**, 133–140.

Yamakawa, J., Henmi, C. and Kawahara, A. (1993) Synthesis and X-ray studies of kimzeyite, $Ca_3Zr_2(Al,Fe)_2SiO_{12}$. *Mineralogical Journal*, **16**, 371–377.

Zaitsev, A.N., Williams, C.T., Britvin, S.N., Kuznetsova, I.V., Spratt, J., Petrov, S.V. and Keller, J. (2010) Kerimasite, $Ca_3Zr_2(Fe_2^{3+}Si)O_{12}$, a new garnet from carbonatites of Kerimasi volcano and surrounding explosion craters, Northern Tanzania. *Mineralogical Magazine*, **74**, 803–820.

https://doi.org/10.1180/minmag.2015.079.3.15 Published online by Cambridge University Press